Soft Matter

Accepted Manuscript

This is an *Accepted Manuscript*, which has been through the Royal Society of Chemistry peer review process and has been accepted for publication.

Accepted Manuscripts are published online shortly after acceptance, before technical editing, formatting and proof reading. Using this free service, authors can make their results available to the community, in citable form, before we publish the edited article. We will replace this *Accepted Manuscript* with the edited and formatted *Advance Article* as soon as it is available.

You can find more information about *Accepted Manuscripts* in the Information for Authors.

Please note that technical editing may introduce minor changes to the text and/or graphics, which may alter content. The journal's standard Terms & Conditions and the Ethical guidelines still apply. In no event shall the Royal Society of Chemistry be held responsible for any errors or omissions in this *Accepted Manuscript* or any consequences arising from the use of any information it contains.

ROYAL SOCIETY OF CHEMISTRY

www.rsc.org/softmatter

Journal Name

ARTICLE TYPE

Cite this: DOI: 10.1039/xxxxxxxxxx

Dynamics of a disc in a nematic liquid crystal †

Alena Antipova,*[a] and Colin Denniston*,‡[b]

Received Date
Accepted Date

DOI: 10.1039/xxxxxxxxxx

www.rsc.org/journalname

We use lattice Boltzmann simulations to study the dynamics of a disc immersed in a nematic liquid crystal. In the absence of external torques, discs with homeotropic anchoring align with their surface normal parallel to the director of the nematic liquid crystal. In the presence of a weak magnetic field a ferromagnetic disc will rotate to equilibrate the elastic torque due to the distortion of the nematic director and the magnetic torque. When the magnetic field rotates the disc so that the angle θ between normal to the surface of the disc $\hat{\mathbf{a}}$ and director of the liquid crystal $\hat{\mathbf{n}}$ becomes greater than $\pi/2$, the disc flips around the axis perpendicular to the rotation axis so that $\hat{\mathbf{a}}$ sweeps through π radians. An analysis of this behaviour was performed. In particular, we look at the impact of the disc thickness and edges on defect creation and the flipping transition. We also analyse the importance of backflow.

1 Introduction

In the 1990s a novel class of composite materials was discovered examining suspensions of colloidal particles in liquid crystals[1–8]. Their properties arise because of the existence of unique long-range interactions between colloidal particles in liquid crystal medium that are not presented in isotropic fluids. These interactions have their origin in the coupling between colloidal particles and the orientation of liquid crystal molecules. When an inclusion is added to the liquid crystal, interactions at the particle surface impose boundary conditions on the orientation of the liquid crystal particles close to the particle surface, leading to a distortion of the director field and, possibly defects, thus increasing the elastic energy of the medium[4,5,9]. The particles can share regions of distortion and defects to lower the energy[10,11]. This can result in a short range attraction between particles which may be different in character from the long-range forces. This provides opportunities for organization and manipulation of colloids and leads to strategies for formation of self-assembled structures and ways of fabricating metamaterials[5,6,12–17]. Structures of self-assembling particles can be applied in photonic, optoelectronic, as well as in chemical and biological sensing[16,18–23].

The majority of experimental and numerical research on self-assembling inclusions has been performed on spherical particles[8,11,12,16,23], rod-shaped particles[24–30], or prolate spheroidal colloids[31–33], although some studies have considered more complicated shapes[34,35]. Electrical or magnetic fields can be used to manipulate colloids, controlling their motion and organization. For example, spherical particles are often manipulated through laser traps, although the required electrical fields also affects the liquid crystal alignment[24]. On the other hand, experiments on ferromagnetic nanowires immersed in liquid crystals have used magnetic fields for particle manipulation instead. The required magnetic fields are small ($< 10G$) enough[27] to avoid changing the alignment of the liquid crystal particles[36]. In contrast to spherical particles, the orientation of an aspherical inclusion with respect to the liquid crystal director plays an important role, since any changes in the inclusion's orientation affects the total elastic energy of the system. As a result, the particle experiences a torque that makes it rotate to the position of the lowest distortion energy, where elastic torque and magnetic torque are balanced. It has been shown that the torque on a rod-shaped colloid with parallel anchoring follows a linear dependence on the orientation of the particle[27] and the elastic energy changes with analogy with electrostatic field energy[37], at least for small to moderate distortions. This implies that the rod will exhibit angular motion under the action of a magnetic field until it rotates by approximately π from its original position; then the rod precesses to release the distortion in the liquid crystal. According to the latest experiments[38], a disc with perpendicular anchoring under similar conditions firstly behaves similarly and demonstrates angular motion, but the release of the liquid crystal distortion through flipping happens much earlier, closer to $\pi/2$.

For a better understanding of this complicated motion and associated properties of the disc-shaped inclusion and liquid crystal, we have performed 3D simulations of the behaviour of an isolated

* Department of Applied Mathematics, The University of Western Ontario, London, Ontario N6A 5B8, Canada
‡ Department of Physics and Astronomy, The University of Western Ontario, London, Ontario N6A 5B8, Canada
[a] E-mail: aantipov@uwo.ca
[b] E-mail: cdennist@uwo.ca

† Electronic Supplementary Information (ESI) available. See DOI: 10.1039/b000000x/

ferromagnetic disc with homeotropic anchoring in a nematic liquid crystal in the presence of a rotating weak magnetic field. The aim of this work is to investigate ways of controlling the motion and the director field distortion around the immersed particle through the disc size and properties of the magnetic field, such as its angular speed and magnitude. We also examine the role of the edge of the disc in defect generation, the flipping transition, and backflow effects (the effects of coupling between the liquid crystal director field and the velocity field) on the motion of the disc. In addition to seeing a simple flipping behaviour similar to the one from the experiment, we observe and analyse more complicated situations when the disc demonstrates a mix of flipping motion and rotational motion of the face of the disc. We also observe a different way for the disc to release the distortion rather than to spin in the case of rapidly rotating magnetic fields — by creating a defect line.

2 Modeling

2.1 Equations of motion

The liquid crystal orientation is described in terms of a local tensor order parameter $\mathbf{Q}$. $\mathbf{Q}$ is a traceless symmetric 3x3 matrix with largest eigenvalue $\frac{2}{3}q$, $0 < q < 1$, that describes the magnitude of order along the corresponding eigenvector $\hat{\mathbf{n}}$, called the director. The equilibrium properties of the liquid crystal can be described by a Landau-de Gennes free energy[36]

$$F = \int_V dV\{F_{bulk} + F_{elastic} + F_{MF}\} + \int_{\partial V} dSF_{surf}. \quad (1)$$

Here F_{bulk} is the bulk free energy and $F_{elastic}$ is the elastic free energy terms. These terms are similar to those in[17], and are commonly used in the liquid crystal literature[36,39,40]. The one elastic constant approximation has been used for most of the simulations, although some simulations were done with multiple elastic constants to see the role this anisotropy plays.

The last term in (1) defines a pinning potential on the surface of the disc and, therefore, the preferred direction of the liquid crystal particles on the surface

$$F_{surf} = \frac{1}{2}\alpha_s(Q_{\alpha\beta} - Q^0_{\alpha\beta})^2, \quad (2)$$

where $\mathbf{Q}^0$ has the form $Q^0_{\alpha\beta} = q^0\langle n^0_\alpha n^0_\beta - \frac{1}{3}\delta_{\alpha\beta}\rangle$. Here $\hat{\mathbf{n}}^0$ is a preferred orientation of the liquid crystal particles on the surface of the disc, q^0 is set to the equilibrium bulk value and $\alpha_s > 0$ (for homeotropic anchoring) defines the strength of pinning (for strong pinning $Q \approx Q^0$ on the surface).

The free energy density F_{MF} of the nematic in the presence of magnetic field $\mathbf{B}$ is linear in $\mathbf{Q}$ and is written as[41]

$$F_{MF} = -\frac{1}{3}\mu_0\Delta\chi^{max}B_\alpha Q_{\alpha\beta}B_\beta - \frac{1}{6}\mu_0\chi_{\gamma\gamma}, \quad (3)$$

with $\boldsymbol{\chi}$ being the diamagnetic tensor, $\Delta\chi^{max}$ being maximal anisotropy and μ_0 is the magnetic permeability of vacuum. For our simulations, $\mathbf{B}$ is tiny so that F_{MF} is negligibly small and does not change the orientation of liquid crystal molecules.

The order parameter $\mathbf{Q}$ evolves according to the convection-diffusion-like equation[40]

$$(\partial_t + \mathbf{u}\cdot\nabla)\mathbf{Q} - \mathbf{S}(\mathbf{W},\mathbf{Q}) = \Gamma\mathbf{H}, \quad (4)$$

where $\mathbf{u}$ is bulk fluid velocity and Γ is a rotational diffusion constant, and $W_{\alpha\beta} = \partial_\beta u_\alpha$. The first term on the left-hand side of this equation is the material derivative that describes the time dependence. The second term, the form of which is same as in[17], appears in the equation because the particles of the liquid crystal are usually of rod-like form and, therefore, the order parameter distribution can be both stretched and rotated by the flow gradients. The term on the right-hand side of (4) describes the relaxation of the tensor order parameter towards the minimum of the free energy. The molecular field $\mathbf{H}$, related to the variational derivative of the free energy, provides the driving force

$$\mathbf{H} = -\frac{\delta F}{\delta Q} + \frac{1}{3}\mathbf{I}Tr(\frac{\delta F}{\delta Q}). \quad (5)$$

Liquid crystals also obey the Navier-Stokes equations

$$\begin{aligned}(\partial_t\rho + \partial_\alpha\rho u_\alpha) =& 0,\\ \rho\partial_t u_\alpha + \rho u_\beta\partial_\beta u_\alpha =& \partial_\beta\tau_{\alpha\beta} + \partial_\beta\sigma_{\alpha\beta} + \\ & \eta_{iso}[\partial_\beta(\partial_\alpha u_\beta + \partial_\beta u_\alpha)],\end{aligned} \quad (6)$$

where ρ is the density, $\mathbf{u}$ is the velocity, $\eta_{iso} = \frac{\rho\tau_f}{3}(\frac{\Delta x}{\Delta t})^2$ is the isotropic "part" of viscosity, and Δx and Δt are discrete space and time steps. The stress tensor given below can be mapped to the Leslie-Ericksen model with five different viscosities[42].Here the stress tensor has a symmetric part

$$\begin{aligned}\sigma_{\alpha\beta} =& -P_0\delta_{\alpha\beta} - \xi H_{\alpha\gamma}(Q_{\gamma\beta} + \frac{1}{3}\delta_{\gamma\beta})\\ & - \xi(Q_{\alpha\gamma} + \frac{1}{3}\delta_{\alpha\gamma})H_{\gamma\beta} + 2\xi(Q_{\alpha\beta} + \frac{1}{3}\delta_{\alpha\beta})Q_{\gamma\varepsilon}H_{\gamma\varepsilon}\\ & - \partial_\beta Q_{\gamma\nu}\frac{\delta F}{\delta\partial_\alpha Q_{\gamma\nu}},\end{aligned} \quad (7)$$

where ξ is a constant that depends on the molecular details of the liquid crystal (i.e. aspect ratio of the particles). In addition, as liquid crystals can transmit torque, there is an antisymmetric part

$$\tau_{\alpha\beta} = Q_{\alpha\gamma}H_{\gamma\beta} - H_{\alpha\gamma}Q_{\gamma\beta}. \quad (8)$$

Parameters used in our simulations are given in Table 1. These equations are modeled on a uniform grid using the lattice-Boltzmann algorithm as described in Appendix A.

2.2 Object representation and implementation of forces

We simulated a disc with radii R and thickness L (see table 1) in two ways. In the first case (see Figure 1a) the object was represented by equally distributed nodes on the bases of the cylinder with the distance between bases equal to the thickness of the disc (referred to later as the "edgeless" representation). The second representation, referred to as the "edged" representation, consisted of the same nodes plus nodes on the cylindrical surface (see Figure 1b). There are two reasons to examine these different

Table 1 The simulation parameters used are given here.

Symbol	Value	Units
LC parameters		
A_0	0.5	atm
γ	3.2	—
K_1, K_2, K_3	9.5, 5.1, 13.8	pN
$K_1 = K_2 = K_3 = K$	10.72 *or* 15.0	pN
Γ	0.33775	$(atm \cdot \mu s)^{-1}$
ξ	0.75 *or* 0.52	—
dx	0.0625	μm
Δt	1	μs
P_0	1.0	atm
$\tau_f/\Delta t$	0.56	—
$\tau_G/\Delta t$	0.25	—
Disc		
radii R	0.21—2.4	μm
thickness L	0.0308—0.21	μm
number of nodes	298—40162	—
strength of anchoring α_s	0.2—0.9	—

representations.

The first reason is that in the physical implementation (i.e. the experiment) the effective boundary conditions on the face of the disc should be well represented by a term such as eqn.(2) with the preferred orientation normal to the surface. As homeotropic anchoring is typically obtained by chemical treatment of the surface, it is not clear how effective this treatment is on the edge of a very thin disc. That is, if the homeotropic anchoring was perfect on the edge one should have a defect around the disc edge even in the case when the disc's orientation does not produce any distortion due to the conflict between the face and edge conditions for the director on the surface of the disc. On the other hand, if the anchoring on the edge of the disc was weak, the molecules may avoid a defect along the edge and align perpendicularly to the face, even along the edge. Our two representations model the two extremes where the edgeless case is equivalent to assuming the disc is too thin for effective chemical coating and the edged case strictly enforces the normal anchoring on the edge of the disc, which should be the case for thicker discs. For intermediate edge anchoring strengths we find that the system effectively adopts a director configuration that is similar to one of the two extreme cases we study here. For example, if the edge anchoring is sufficiently weak, the system just adopts the director configuration of the edgeless disc but with some loss of order near the edge (i.e. the magnitude of q decreases). Conversely, if the edge anchoring is sufficiently strong, it generates a defect which is always pinned to the edge, similar the edged representation.

Since, for the edgeless case, we don't have any particles on the cylindrical surface, in order to recover an imposed value of Q from the disc onto the Lattice Boltzmann mesh, the thickness of the object should be in the range $0 < L < 2dx$, where dx is the size of the grid cell. Thus this type of representation can be used for thin discs and laths. The advantage of the second case of the representation is that we can specify the conditions on the cylindrical surface, hence, there is no constraints on the thickness

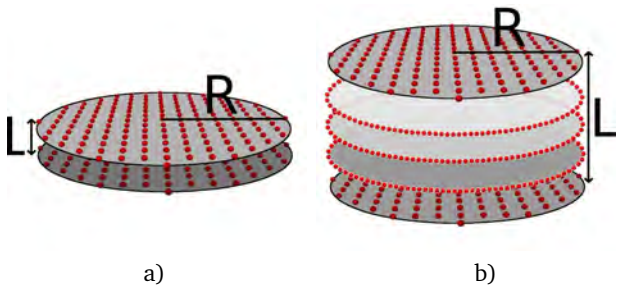

Fig. 1 Schematic representation of the disc in the simulation (colour online): a) The disc is represented only by bases; b) Additional points on the cylindrical surface have been added.

of the object and one can use this representation for cylindrical colloids such as wires and rods. However this requires slightly more computational time due to a larger number of points in the object representation.

We then distribute nodes to nearby lattice mesh sites by assigning weights $\zeta_{\alpha j} = \phi_j(x_\alpha)\phi_j(y_\alpha)\phi_j(z_\alpha)$ to these sites using a trilinear stencil. This sets the weight to the nearest sites according to $\phi_j(r_\alpha) = 1 - |\Delta r|$ with $\Delta r = (r_\alpha - r_j)/dx$, where r_α and r_j are the position of a node and lattice mesh site, respectively[43].

The preferred anchoring at the surface of the disc implies a net torque $\mathbf{\Gamma}$ from the liquid crystal to the disc:

$$\Gamma_\alpha = -\sum_i 2\tau^{SC}_{\beta\gamma}\Delta V_i, \tag{9}$$

where α, β, γ are cyclic permutations, $\tau^{SC}_{\beta\gamma}$ is similar to (8) but contains only molecular field from surface anchoring (2), $\mathbf{H}^{SC} = \alpha_s(\mathbf{Q} - \mathbf{Q}^0)$, the sum is over the nodes i on the disc surface, and ΔV_i is a local volume element.

When the disc moves through the liquid crystal, hydrodynamic forces arise. We simulate these by applying equal and opposite forces to mesh sites and nodes of the colloidal disc:

$$\mathbf{F} = \lambda(\mathbf{v}_n - \mathbf{u}_f), \tag{10}$$

where $\mathbf{v}_n$ is a particle node velocity and $\mathbf{u}_f = \sum \mathbf{u}_j \xi_{j\alpha}$ is the velocity of the fluid interpolated to the particle node location. Here λ is set to

$$\lambda = \frac{2m_u m_v}{\tau_f(m_u + m_v)}, \tag{11}$$

where m_u and m_v are masses of the particle node and representative fluid mass at the node location, respectively. See Ref.[43],[44] for detailed information.

In sections 3.2.1 and 3.2.2 two different cases are examined: with backflow effects being switched off; and with backflow taken into account. For each simulation there is a specification in the text and/or picture what case is being examined. The purpose of investigating both cases is to determine whenever the backflow can be neglected or not in this type of simulations and examine the effects of backflow on disc's dynamics.

Net surface anchoring forces appear due to the distortion in the liquid crystal director field and are calculated according to

$$F_\alpha = \sum_i n_\beta \sigma^{SC}_{\alpha\beta}\Delta S_i, \tag{12}$$

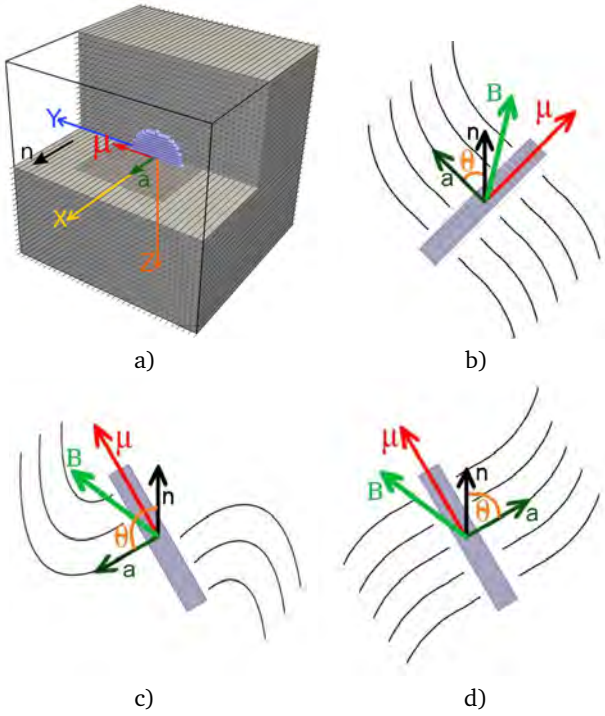

Fig. 2 Schematic representation of a disc with perpendicular anchoring (colour online): a) No external forces are acting on the system; b) Disc is rotated by $\theta < \frac{\pi}{2}$; c) Director field is highly distorted when the disc is rotated by $\theta > \frac{\pi}{2}$ and is about to flip; d) configuration is stable after the transition. Pictures b-d, adapted from [38], are top views.

where $\sigma^{SC}_{\alpha\beta}$ is based on (7) with $\mathbf{H}$ replaced by $\mathbf{H}^{SC}$, ΔS_i is the portion of the surface of the colloidal particle represented by node i, and $\hat{\mathbf{n}}$ is a surface normal. The calculations are performed not directly at the node location, but at the outer edge of the surface, by stepping out one lattice Boltzmann distance unit, dx, along the surface normal [10]. In the cases here, the net surface anchoring forces make no differences: there is no centre-of-mass motion of the disc. However, the net torque arising from the surface anchoring, Eq.(9) is crucial to the disc motion.

An additional torque $\mathbf{T}_{MF} = \boldsymbol{\mu} \times \mathbf{B}$ from the magnetic field $\mathbf{B}$ was applied to the disc. Here $|\boldsymbol{\mu}| = (0.32 \pm 0.06) \times 10^{-13}\mathrm{A \cdot m^2}$ is the magnetic moment of the disc which is in the plane of the disc surface (see Figure 2). The value of magnetic moment was set to be proportional to the experimental value: both the size of the disc and its magnetic moment was taken to be about 50 times smaller than in the experiment [38]. The magnitude of the magnetic field $\mathbf{B}$ was in the range 0.001 G – 0.2 G.

The algorithm described above was implemented using LAMMPS [45] with use of a fix similar to one given by Mackay *et.al.* in [44] modified to describe liquid crystal dynamics. In the lattice Boltzmann method, $\mathbf{H}$ enters the driving term in the calculation of (20) and (22) for the case when backflow effects are off. However, when we have backflow, in order to prevent double counting of part of the hydrodynamic forces, the distribution function f_i (fluid part) contains only $\mathbf{H}$ from (5), while $\mathbf{G}_i$ (liquid crystal part) has both molecular field related to the variational derivative of the free energy and molecular field from the surface anchoring. Surface anchoring net force (12) contains only $\sigma^{SC}_{\alpha\beta}$ since the bulk fluid stress effects are already included into hydrodynamic stress tensor which will move fluid and hence the disc due to the no-slip condition imposed by Eq. (10).

Parameters used in the simulations are provided in table 1. The simulation domain in each direction was at least 6 times bigger than the radius of the disc to reduce boundary effects. We tested a small number of simulations with a larger box and found no qualitative difference. The xy-plane had periodic boundaries in both directions. Rigid walls were located at $z = -l/2$ and $z = l/2$, where l is the height of the domain. Boundary conditions on the walls, director along the x-axis, will result in equilibrium conditions for the director of $\hat{\mathbf{n}} = (1, 0, 0)$ throughout the simulation domain. A disc with homeotropic anchoring on the surface was initially placed in the middle of the domain with its normal also along the x-direction (Figure 2a; later figures show the top views of the shaded section). The magnetic field starts along the y-direction ($\vartheta_{MF} = 0^\circ$, also the direction of magnetic moment of the disc) and then rotates in the xy-plane by a small amount, 0.0001°–0.05° every time step or 0.28 Hz–139 Hz, until it reaches the final position $\vartheta^{stop}_{MF} \in [120^\circ, 180^\circ]$.

3 Results

3.1 Capacitance measurements

We first investigate the situation for small rotations. Without any external forces, a disc with homeotropic anchoring aligns itself in such a way that the surface normal $\hat{\mathbf{a}}$ is parallel to the far field director $\hat{\mathbf{n}}$ (Figure 2a). There is no distortion observed in the liquid crystal except for the distortion around the edges for the edged representation due to the conflict between surface conditions. When the magnetic field $\mathbf{B}$ is switched on, $\mathbf{B}$ is parallel to $\boldsymbol{\mu}$ initially (along positive direction of y-axis), and then starts turning, the nickel disc reacts to it and rotates to an angle θ (angle between $\hat{\mathbf{n}}$ and $\hat{\mathbf{a}}$) at which all torques are balanced, leading to a distortion of the director field (see Figure 2b) that costs elastic energy. This distortion appears in order to satisfy the homeotropic anchoring conditions on the surface of the disc and adds an elastic torque $\tilde{\Gamma}$ to the system.

When $\mathbf{Q}$ is uniaxial, defect-free, and in the one-elastic constant K approximation, the equations for static equilibrium can be linearized and solved in analogy to the electrostatic field energy of an object in a fixed potential [36,46,47] (see Supplementary material for details). This analogy [24,26,27] predicts that the elastic energy varies with the angle of orientation θ as

$$U_{elastic} = 2\pi K C \theta^2, \tag{13}$$

where in analogy to electromagnetism, C stands for the "capacitance" of the colloidal particle. For an oblate spheroid, this gives

$$C = \frac{L}{2}\sqrt{\left(\frac{2R}{L}\right)^2 - 1}\left(\tan^{-1}\left(\sqrt{\left(\frac{2R}{L}\right)^2 - 1}\right)\right)^{-1}. \tag{14}$$

Equation (13) implies a linear dependence between the elastic torque $\tilde{\Gamma} = \frac{\partial U_{elastic}}{\partial \theta}$ and the orientation of the disc defined by θ when there is no out-of-plane distortion.

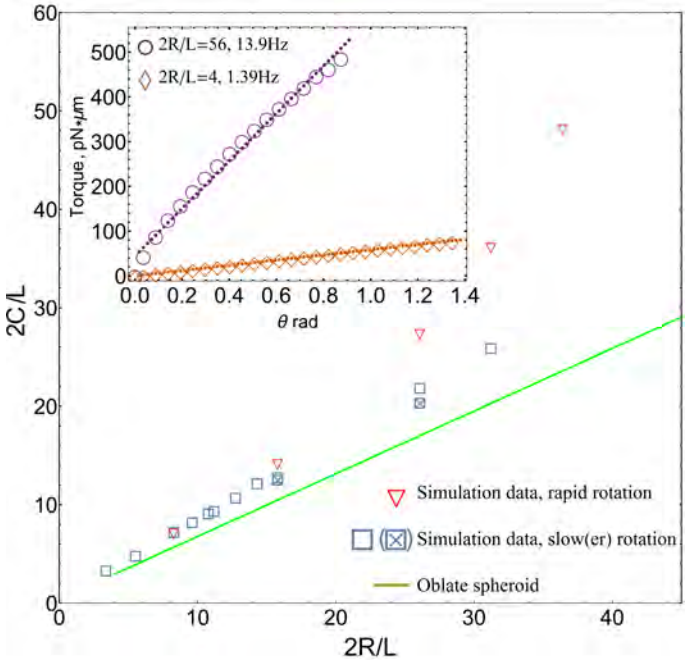

Fig. 3 Capacitance as a function of thickness and radii of the disc. Open markers (triangles and squares) are results from our simulations whereas the line is the analytical prediction of eqn. (14) for an oblate spheroid. For a given $2R/L$, the open triangles correspond to a faster rotation than the open squares, which are faster than the open squares with the x. Inset: The dependence of the elastic torque on the angle θ of rotation of the disc. It is linear when the rotation angle θ is small, disc is small, and the magnetic field is turning slowly (hollow diamonds); if the magnetic field rotates too fast (hollow circles) the linear dependence is violated and that leads to deviations in capacitance (dotted lines shows linear fits).

We test this relationship using simulations with the edgeless disk and one elastic constant, $K = 15.0$ pN (for all simulations in this section backflow effects are not included as we are examining the static limit). A couple of examples of the resulting torque versus θ are shown in the inset of Figure 3. It can be seen from the inset of Figure 3 that our simulation produces a smooth linear relationship between $\tilde{\Gamma}$ and θ when the magnetic field turns slowly enough (i.e. for $2R/L = 4$, 1.39Hz), i.e. the static limit of elastic energy appears to be achieved. Measuring the slope of the torque $\tilde{\Gamma}$, one can measure the value of the capacitance of the disc using the equations

$$\tilde{\Gamma} = \frac{\partial U_{elastic}}{\partial \theta} = 4\pi KC\theta \Longrightarrow \frac{\partial \tilde{\Gamma}}{\partial \theta} = 4\pi KC. \qquad (15)$$

However, when the magnetic field turns rapidly, this linear dependence is violated (Figure 3, $2R/L = 56,\ 13.9$Hz in the inset) and this formula gives poorer results. The angular velocity of magnetic field where deviations from the static results occur depends on the size of the disc, strength of anchoring on the surface and magnitude of magnetic field. The smaller the disc is, the faster the magnetic field can rotate without violating the linear dependence of elastic torque on θ. For example, for a disc with $R = 0.27\mu m$ and $L = 0.075\mu m$, magnetic field $|\mathbf{B}| = 0.06G$ that rotates at $0.005^\circ/\mu s$ a linear dependence is found, but the same magnetic field acting on a disc with $R = 2.07\mu m$ and $L = 0.075\mu m$ results in a non-linear dependence. The non-linearities are a result of the fact that the simulations include the dynamics, resulting in hydrodynamic effects that are dependent on the size of the disc and its rotational velocity. Figure 3 shows the results of simulations (symbols) with discs of different radii R and thickness L (R varied from $0.2\mu m$ to $2.4\mu m$ while L varied from $0.075\mu m$ to $0.21\mu m$). In all cases, a linear fit of the values of $\tilde{\Gamma}$ versus θ obtained in the simulation was used to obtain the capacitance, using the known elastic constant (i.e. this is an "average" slope when $\tilde{\Gamma}$ versus θ is non-linear). The solid line gives the formula for the capacitance of the oblate spheroid (14). It can be seen from Figure 3 that the simulations for small discs ($2R/L < 30$) give good agreement with the theoretical predictions. But discs of bigger radius require the magnetic fields to turn more slowly to satisfy the linear dependence of torque with respect to θ and determine a capacitance in agreement with theoretical predictions, which essentially assumes a static director field (compare squares with triangles). Figure 3 for the most slowly rotating discs does give a linear dependence of $2C/L$ on $2R/L$, although the effective capacitance is slightly larger for the edgeless disc than for the oblate spheroid. We have taken into account the effects of discretization in Fig. 3 as the discretization "spreads" the disc nodes making it effectively slightly larger[48] by about $\Delta x/3$.

If the capacitance of the disc is known, along with the direction and magnitude of the magnetic field, one could measure the rotation of the disc to find the elastic constant K, similar to what has been suggested for rods[24].

3.2 Flip

The equivalence of both directions of the nematic director $\hat{\mathbf{n}}$, $+\hat{\mathbf{n}}$ and $-\hat{\mathbf{n}}$, implies the torque on a colloidal particle in equilibrium should be symmetric about $\theta = \frac{\pi}{2}$. However, the experiments on rods immersed in nematic liquid crystals[27] show that the torque continues to increase linearly as θ increases past $\pi/2$ caused by the metastability and followed by a spin of a wire along its long axis by 180° at $\theta \approx \pi$. In contrast, the disc with homeotropic anchoring under the same conditions behaves differently[38] (see Figure 2c,d). When $\frac{\pi}{2} < \theta < \pi$ the configuration becomes unstable, the surface normal $\hat{\mathbf{a}}$ goes out from the plane of the picture and tilts so that the disc goes through a flipping motion much earlier than a rod.

To study this behaviour of the disc we have looked at the changes in the director field. We were especially interested in possible defects in the liquid crystal that can be seen on the 3D plot by making a density plot of the largest eigenvalue q of the tensor order parameter $\mathbf{Q}$. The results of our simulations are presented in Figures 4, and 9. These figures show the cross-section of the middle part of the simulation domain, viewed from above, with a disc particle in the centre. Figure 4 demonstrates the disc with the edgeless representation (Figure 1a), and Figure 9 has the disc of the edged type (Figure 1b).

3.2.1 Slowly rotating edgeless discs

We now examine the complete rotation of the magnetic field where non-linear effects, such as the disc flipping are evident.

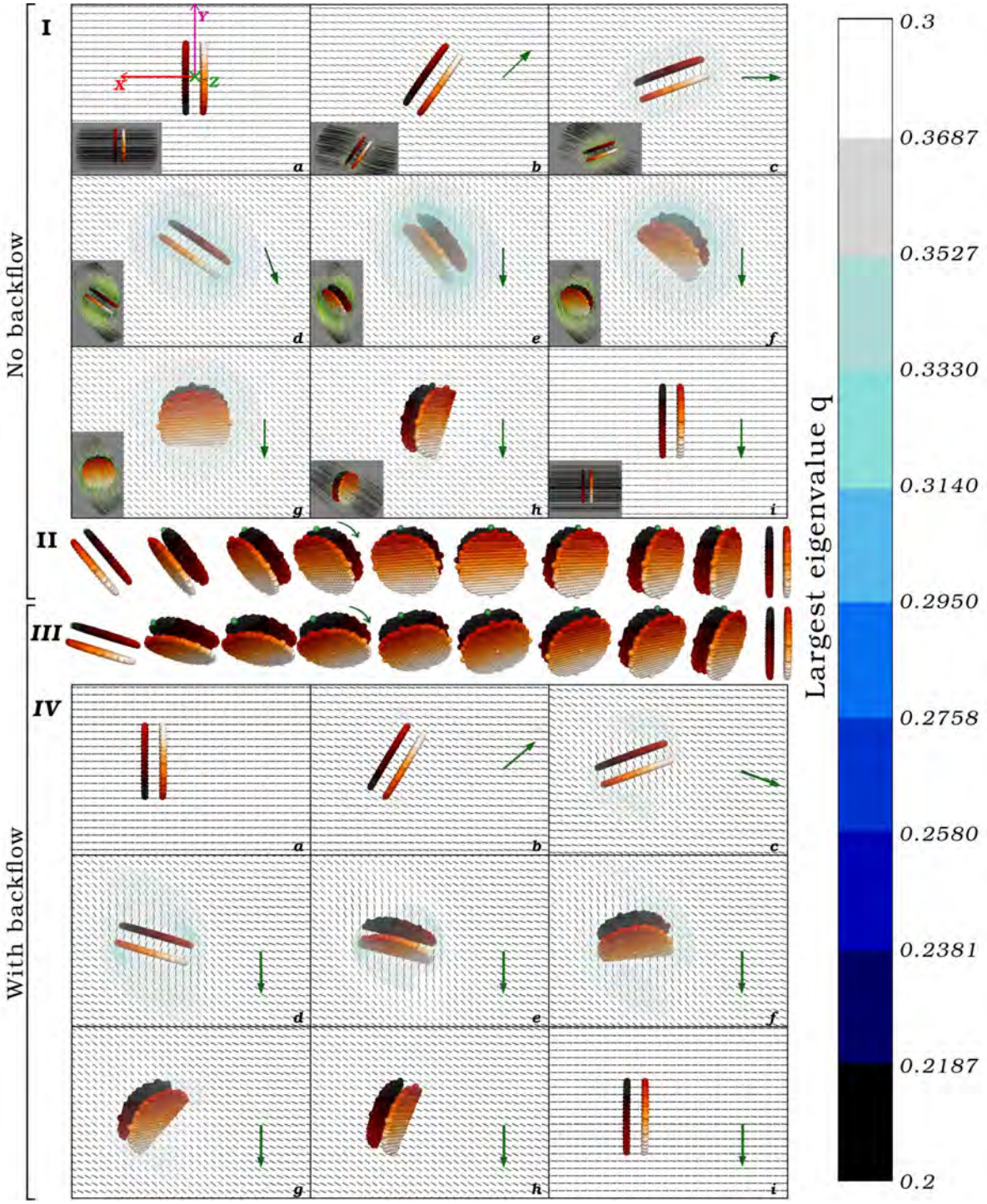

Fig. 4 The simulation of the motion of the edgeless disc under the action of turning magnetic field (colour online). Panels I, II correspond to the case of no backflow, II gives detailed views of the disc motion during the flip; III, IV show the results of the simulation where the backflow effects are on, III shows motion of the disc during the flip. The snapshots are a cross-section near the centre of the simulation domain viewed from above with the disc in the centre (disc is represented by spheres located at the positions of the nodes; the spheres are made about 2 times larger than the real node size for better visibility). Dark blue areas would indicate the position of a disclination line defect, light-blue contour around the disc is a high level of distortion ("softening"), and grey cloud exhibits a light disturbance. The green arrow indicates the direction of the magnetic field. The director appears shorter near the disc in f, g because it is pointing out of the plane. See Supplemental Material for videos of the simulation. The insets in Panel I show director "streamlines" in the vicinity of the disc. These "streamlines" are everywhere parallel to the local director field and demonstrate the director behaviour around the disc during the flip. As can be seen, the motion undoes the bend in the streamlines without breaking or kinking them (ie. no defect is created).

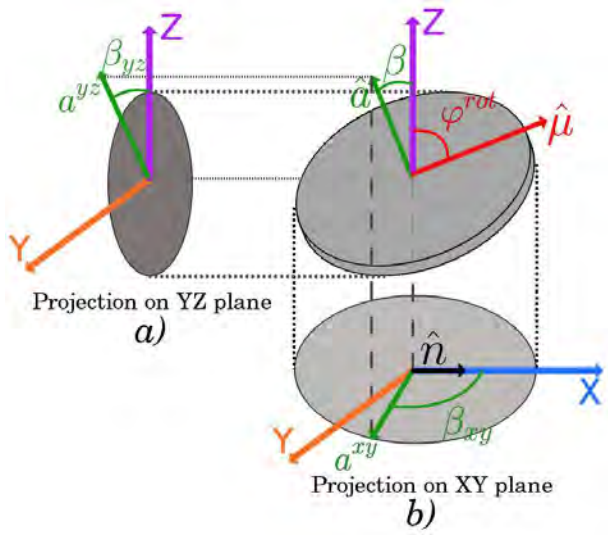

Fig. 5 Schematic explanation of the angles used for motion analysis throughout the article: a) angles related to projecting surface normal $\hat{\mathbf{a}}$ on YZ plane, b) angles related to the projection of $\hat{\mathbf{n}}$ on XY plane.

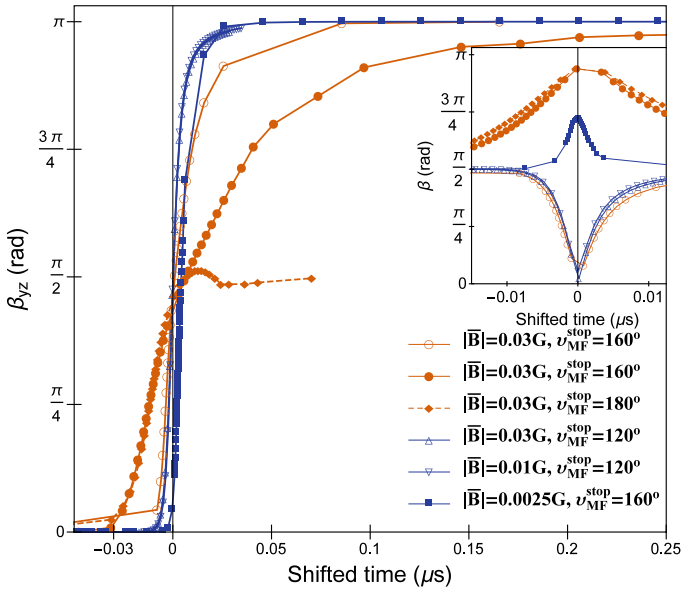

Fig. 6 The dependence of angle β_{yz} on time for different edgeless discs and magnetic fields; inset: angle β for the same simulations. Origin of time is set to the location of the extrema of β.

Here we will focus on 2 specific realizations. Both of them are working with a "small" edgeless disc with $R = 0.3\,\mu m$ and $L = 0.15\,\mu m$ consisting of 634 nodes under the action of the same magnetic field of magnitude $0.005G$ and rotational frequency $0.005°/1\mu s$ (13.9Hz) that rotates by $180°$ from its original position along y-axis. However, the simulation shown in Figure 4I, II does not include backflow effects, while the simulation with results shown in Figure 4III, IV has backflow. Both simulations use the one elastic constant approximation with $K = 10.72pN$. The linear size of the simulation boxes is 6 times larger than the disc radius in all directions.

No backflow. Initially the surface normal of the disc is parallel to the director field and no distortion in the liquid crystal is observed (Figure 4Ia). Then the magnetic field is switched on, initially aligned with the magnetic moment of the disc $\boldsymbol{\mu}$, and starts to turn, followed by the disc rotating, geared towards minimizing the distortion torque as was discussed in the previous section. During this motion the director field around the disc is distorted but no defects are observed (Figure 4Ib and Ic). The disc slows down after getting through $\theta \sim \frac{\pi}{2}$. As θ increases further, the distortion area enlarges, and, at a critical angle θ_{crit}, the disc starts to flip (Figure 4Id and Ie). The "softening" cloud (very slight decrease in the largest eigenvalue, but not enough to create a defect) around the disc during the flip firstly grows and then collapses back on the surface of the disc (pictures e-g in Figure 4I). The final position of the disc corresponds to a less distorted director field and, thus, to a smaller free energy of the system.

Comparison of simulations performed with one elastic constant approximation to simulations where $K_1 \neq K_2 \neq K_3$ on different edgeless discs affected by various magnetic fields shows that the behaviour of the disc is similar, except that the distortion spreads much further from the disc. This is probably due to the fact that for the unequal elastic constants case we examined, K_2 was smaller ($K_2 = 5.1pN$ versus $10.72pN$ in the one-elastic constant case) even though the average elastic constant was similar. The system takes advantage of the weakest elastic constant and concentrates any distortion that can be accommodated by twist rather than splay or bend. Similar effects were found for rods in[24]. An additional effect of this weaker distortion mode is that the disc rotates further before the distortion energy has built up enough to induce a flip. This also takes more time because the disc also rotates more slowly as θ increases. Considering that switching to the one elastic constant approximation does not qualitatively change the main features of the dynamics but saves computational time, all further measurements in this and following sections are performed within this approximation.

To better understand the flipping motion of the disc, we study the time dependence of angles associated with the disc. We first examine the angle β_{yz}, that is the angle between the z-axis and the projection of the surface normal $\hat{\mathbf{a}}$ on the YZ plane, i.e. the plane perpendicular to the far-field director $\hat{\mathbf{n}}$, as was done in the experimental study[38] (see Figure 5a). Results for β_{yz} for different discs and various magnetic fields are presented in Figure 6. It can be seen that our results here are similar to experiments[38]: sigmoidal shape dependence of β_{yz} as a function of time. However, using this angle alone works well only for a description of simple flipping motion with big θ_{crit} and with only insignificant rotational motion of the disc face. For example, in Figure 6, the orange line with filled symbols corresponds to a simulation in which the second half of the flip happens in the XZ plane and results in a different form of the curve; however, using other angles like β (to be introduced below), shown in the inset, demonstrates that this simulation does not actually differ from the others. We found two other angles, β_{xy} and β, more informative for the purpose of our analysis. The first of them, β_{xy}, is the angle between the x-axis and the projection of the surface normal on the XY plane (see Figure 5b). Until the surface normal goes out of plane β_{xy} tracks

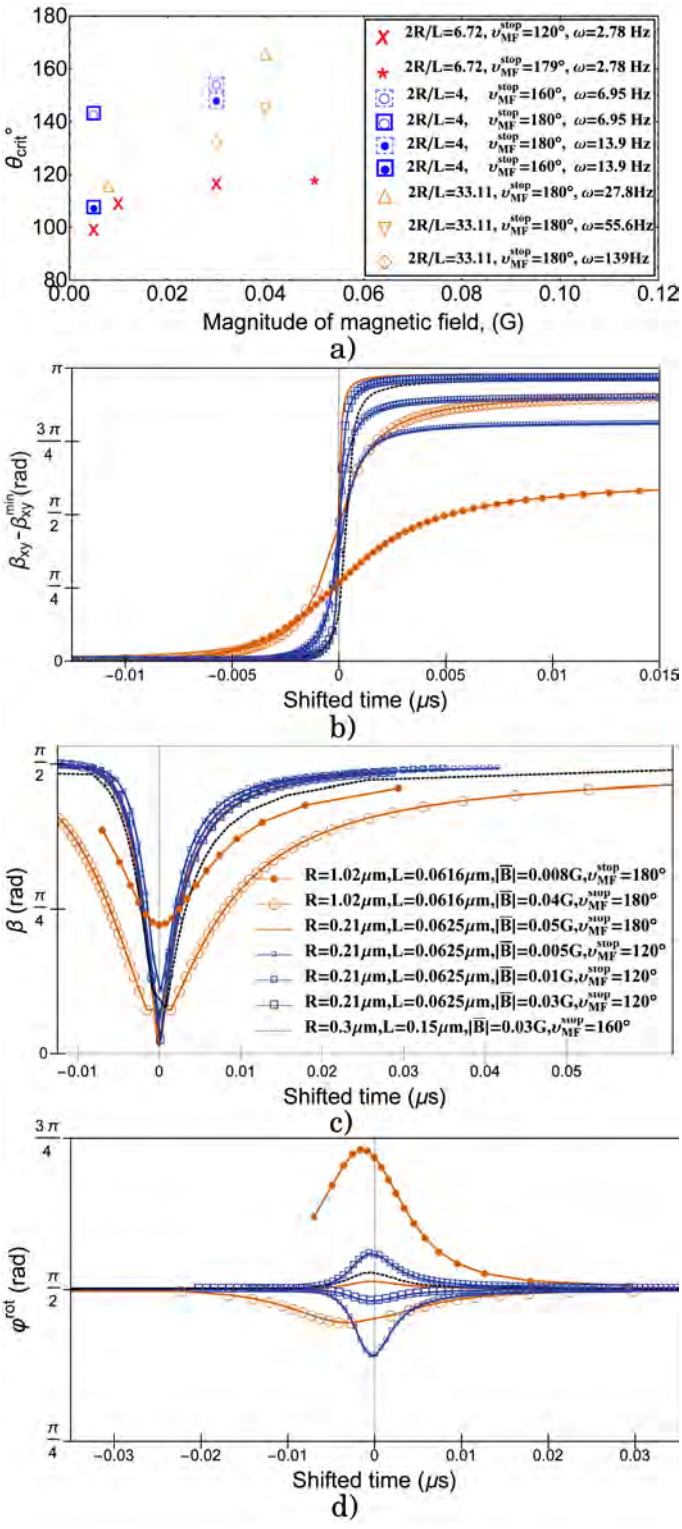

Fig. 7 a) Dependence of the angle at which the disc flips θ_{crit} versus $|\mathbf{B}|$ for different systems. b) The dependence of angle β_{xy} on time for different edgeless discs and magnetic fields. c) The dependence of angle β on time for the same simulations as in b) d)The time dependence of angle φ^{rot} for the same simulations as in b) and c). Time is shifted to have 0 at the minimum of β. Legend for (b)-(c) plots is shown in c).

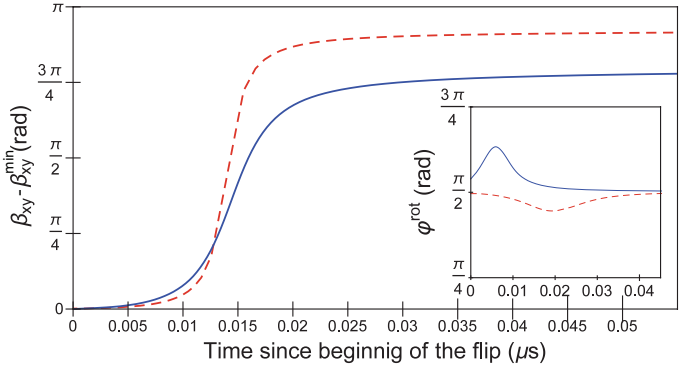

Fig. 8 Comparison of β_{xy} for simulations with/without backflow (colour online). Dashed lines corresponds to no backflow, continuous - with backflow. The simulations are performed on the edgeless disc of $R = 1.02\,\mu m$, $L = 0.0616\,\mu m$ consisting of 7250 nodes under action of magnetic field of magnitude $0.04G$ rotated by $180°$. The inset shows the rotational motion measured by φ^{rot} for the same simulations.

$\pi - \theta$, before increasing again towards π during the flip. Results for this increase are shown on Figure 7b. For the second angle determined by $\beta = \arccos(\hat{\mathbf{a}}.\hat{\mathbf{k}})$, where $\hat{\mathbf{k}}$ is a unit vector along z-axis, results are presented on Figure 7c. One should remember that discs in all simulations do not start to flip at the same time but rather unless otherwise noted, the time scale was shifted to 0 at the minimum (or maximum) value of β (discs can flip both clockwise or counter clockwise) during the flip. The angle at which the disc flips, θ_{crit} is plotted in Figure 7a. θ_{crit} depends on the size of the disc, angular speed and magnitude of magnetic field $|\mathbf{B}|$, and its maximum rotation angle ϑ_{MF}^{stop}. As can be seen, increasing $|\mathbf{B}|$, with other factors constant, generally increases the critical angle (the disc flips later). A weaker trend is seen with increasing angular frequency decreasing θ_{crit}.

In the experiment the magnetic field set-up and abrupt motion implies a symmetric position of the disc just before and right after the flip, i.e. β_{yz} and β_{xy} changes by π, while in our case the positions of the disc before and after the flip are not symmetric due to the difference in the motion of the magnetic field. However, a symmetric flip can be obtained by making the disc go through the flipping motion when $\mathbf{B}$ is parallel to $\boldsymbol{\mu}$ by tuning the magnetic field: by increasing the magnitude of the magnetic field, the disc rotates by π compared to lines with smaller squares that represent the results for weaker magnetic fields (e.g. Figure 7b, squares). The case of a symmetric position of the disc right before and after the flip would correspond to $min(\beta) \to 0$ in Figure 7c. Looking at these plots and comparing the lines with open squares (they correspond to the same simulations except for the magnitude of magnetic fields), we can conclude that by tuning only the magnitude of magnetic field it is possible to control the moment of the flip and the final position of the disc. Also, as seen in Figure 7b, since the inclination of the lines is bigger for stronger magnetic fields, the speed of flipping is higher when the magnitude of the magnetic field is bigger, which means that the flipping is faster for larger θ_{crit} (disc's rotational angle at which flip starts, Fig. 7a). One may also note from Figure 7c that plots are not perfectly

symmetric with respect to $t = 0$. That means that the first half of the flip goes faster, while after getting to the minimum value of β, flipping slows down. This is probably due to the fact that even though there is no backflow, there are hydrodynamic forces and the disc has to push the fluid out of the way during the motion and this is harder in the initial stages of the flip when the fluid is not already moving in the right direction.

Figure 7d demonstrates the rotational properties for the same simulations as in Figure 7b and c. This figure demonstrates that stronger magnetic fields acting on the discs provoke more rotation and that discs can flip both ways (compare, for example, the line with hollow circles with filled circles line and lines with empty squares). From this picture we can also conclude that an edgeless discs φ^{rot} tends to go to $\pi/2$ at the end of simulation, meaning that there is no tilt in the disc position in the end.

With backflow. All the results demonstrated above do not include backflow effects, which means the orientation of the liquid crystal particles does not affect the velocity field. However, as demonstrated in[49] and[50], backflow may play a significant role in the motion. By visual comparison of Figure 4I and Figure 4IV, it is easy to see that there are differences in results for simulations without backflow effects and with them, although the qualitative flipping behaviour is present in both simulations. First, the distortion cloud around the disc during the flip for with backflow case is smaller (lighter colouring of the density plot of the largest eigenvalue of tensor order parameter $\mathbf{Q}$ corresponds to less disorder) because backflow effects allow the disc to move fluid to relax the distortion. This appears to result in more rotation in the plane of the face of the disc (rotation is easy to see from figures II and III in Figure 4). Second, θ_{crit}, that describes the position of the disc right before the moment when the flip begins, is different: compare Figure 4Id with Figure 4IVd and snapshots of disc position in Figure 4II and III. By looking at this figure and tracking the motion of specially marked green particle, one notices that the lower row III (that includes backflow effects) demonstrates not only flipping but also a distinguishable rotational motion of the disc face. To measure quantitatively this face rotational behaviour, we plot time dependence of $\varphi^{rot} = \arccos(\frac{\boldsymbol{\mu}.\hat{\mathbf{k}}}{|\boldsymbol{\mu}|})$, where $\hat{\mathbf{k}}$ is again a unit vector along z-axis (see Figure 5). The inset of Figure 8 compares the level of rotation for similar simulations with and without backflow. It can be seen that backflow forces stimulate more rotational motion of the disc face. On the graph of β_{xy} with respect to time in Figure 8, we can compare the dashed line (without backflow) to the solid line (with backflow effects): there is a significant difference in results that emphasise the necessity of backflow for accurate predictions of disc's motion. Though results without backflow provide qualitatively similar flipping behaviour, to predict the moment of the beginning of the flip and position of the disc after it, backflow effects are vital.

3.2.2 Slowly rotating edged discs

In this section we look in detail at 2 simulations. The first one corresponding to Figure 9I & II has an edged disc of $R = 0.3\,\mu m$ and $L = 0.09\,\mu m$ that consists of 634 nodes; the disc is under the action of a rotating magnetic field of magnitude $0.0025G$ that rotates at $0.001^\circ/1\mu s$ (2.78Hz) and stops at 160° with respect to $+y$-axis. This simulation does not include backflow effects and uses the one elastic constant approximation with $K = 10.72pN$. The discs centre-of-mass does not move appreciably during the simulation implying that the net force remains negligibly small. The linear size of the simulation boxes is 6 times larger than the disc radius in all directions. The second simulation, results of which are shown in Figure 9III & IV works with the same disc and same magnetic field, but has backflow acting on the system. Both discs demonstrate flipping behaviour similar to edgeless discs described in the previous section: at the beginning of the simulation the surface normal $\hat{\mathbf{a}}$ is parallel to the far-field director $\hat{\mathbf{n}}$; when the magnetic field is switched on, the disc follows its rotation (Figure 9Ib-d and Figure 9IVb-d) and then flips to reduce the free energy of the system (Figure 9Ie-i and Figure 9IVe-i).

These simulations indicate that there are no line defects observed in the liquid crystal except for on the edge of the disc (due to the conflict between the surface conditions on the bases and on the cylindrical surface, not present on the edgeless representation). Further, the presence of the defect line around the edged disc results in less distortion away from the disc, compared to the edgeless representation (see, for example, Figure 4Ie versus Figure 9Ie). As the disc flips, there is a spherical region around the disc where the director tilts out of plane to accommodate the normal anchoring on the face of the disc. For the edged representation, with the defect line, this spherical region has almost exactly the same radius as the disc itself (Figure 9If), whereas for the edgeless representation this region is quite a bit larger than the disc (seen in Figure 4Ig). This has to do with the way the distortion is handled by the edgeless disc. In the absence of a disclination line, there is a flattened S-shaped (or O-shaped) distortion with the middle of the S tangential to the disc edge (c.f. Figure 4Ic-f Figure 4IVc-f). This is in contrast to the edged configuration where the presence of the disclination localizes the distortion right at the disc edge. These observations appear, at first glance, to potentially be at odds with the experiments[38] where a defect line seems to appear. We do not believe this to be the case, however, and will discuss this in more detail in Section 3.3.

The time dependence of the angles β_{xy} and β for simulations performed without backflow dynamics, shown in Figure 10a demonstrates, similar to the edgeless discs, that the speed of the flip is higher for a bigger magnetic field. However, for strong magnetic fields that were rotated by 180° (lines with two largest circle markers shown in red and purple), hydrodynamic effects that are not observed in simulations for edgeless discs can be seen: the disc overshoots after it reaches its maximum β_{xy}, similar to the effect of optical bounce described in[51]. However, Figure 10a shows this is not the case for (i) fields rotated by a smaller angle, i.e. by 120° or 160°: see line without markers; (ii) and weaker magnetic fields, whatever the final position of the magnetic field is (compare the two lines with the smallest circle markers). Results for $\beta = \arccos(\hat{\mathbf{a}}.\hat{\mathbf{k}})$ in Figure 10b demonstrate that discs may flip both clockwise and counter clockwise. This implies that edged discs are very sensitive to even small changes in distortion. Also, edged discs tend to stay a bit tilted in their final position when $\vartheta_{MF}^{stop} = 180^\circ$ (β is not tending to reach $\pi/2$, while edgeless discs are approaching $\pi/2$, as seen in Fig 7d).

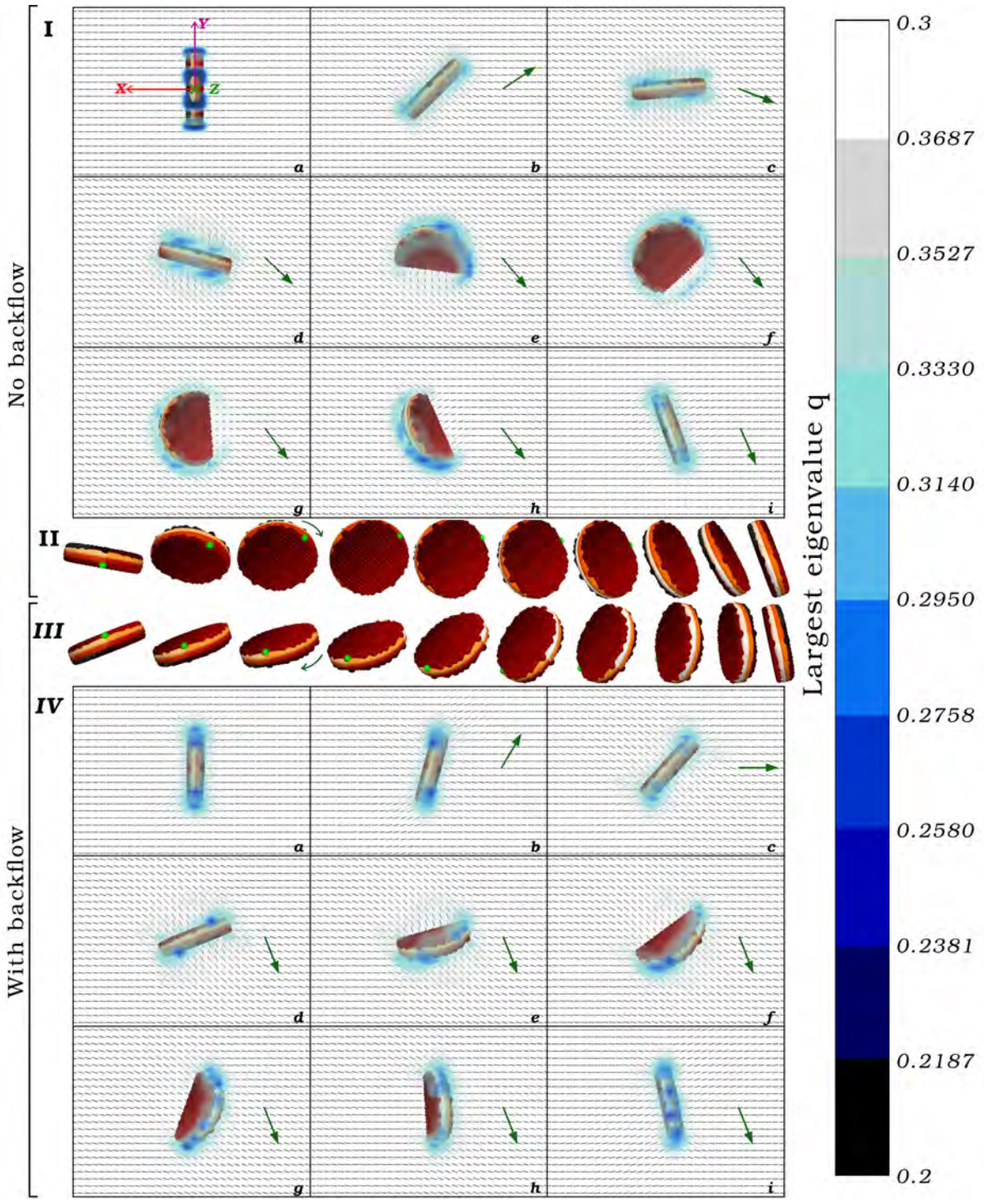

Fig. 9 The simulation of the motion of the edged disc under the action of turning magnetic field (colour online). Pictures I, II correspond to the case of no backflow, II gives detailed views of the disc motion during the flip; III, IV demonstrate the results of the simulation where the backflow effects are on, III shows motion of the disc during the flip. The snapshots are a cross-section near the centre of the simulation domain viewed from above with the disc in the centre (disc is represented by spheres located at the positions of the nodes; the spheres are made about 2 times larger than the real node size for better visibility). Dark blue areas indicate the position of a disclination line defect (discontinuities in this line are a result of a graphic projection: the line is a physically continuous loop around the edge of the disc), light-blue contour around the disc is a high level of distortion ("softening"), and grey cloud exhibits a light disturbance. The green arrow indicates the direction of the magnetic field. The director appears shorter near the disc in e-g because it is pointing out of the plane. See Supplemental Material for videos of the simulation.

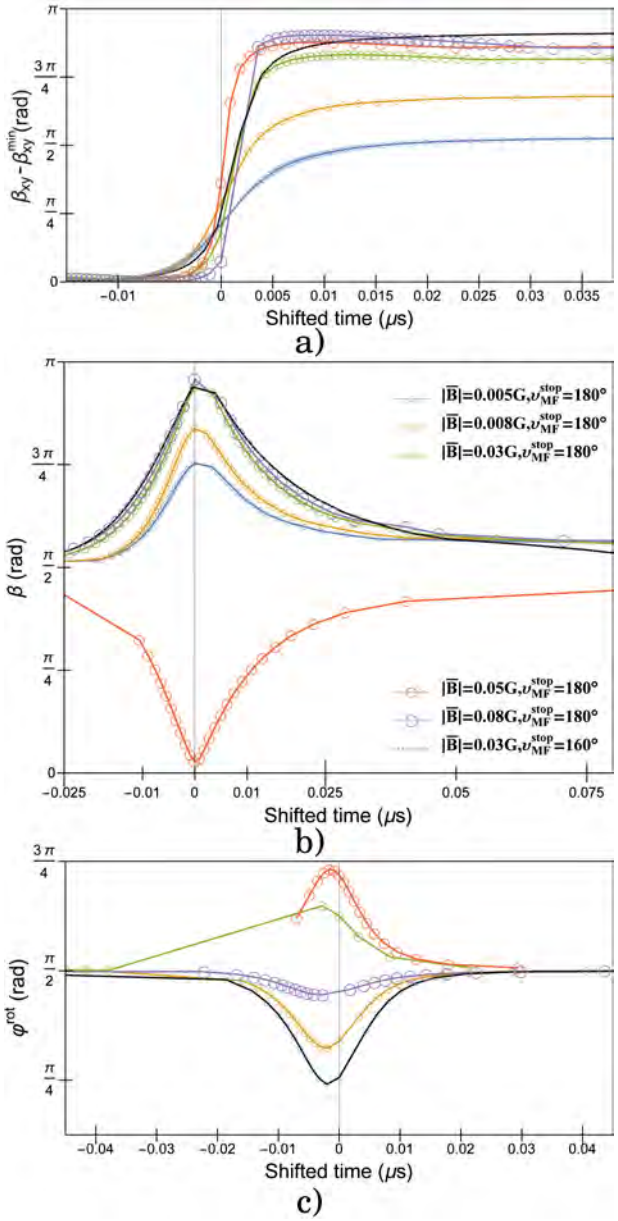

Fig. 10 The dependence of the angles (a) β_{xy}, (b) β, and (c) φ^{rot} on time for different magnetic fields acting on the edged disc of $R = 1.02\,\mu m$, $L = 0.0616\,\mu m$ consisting of 8534 nodes. Time is shifted to have 0 at the minimum of β in all cases and the legend for all plots is shown in b).

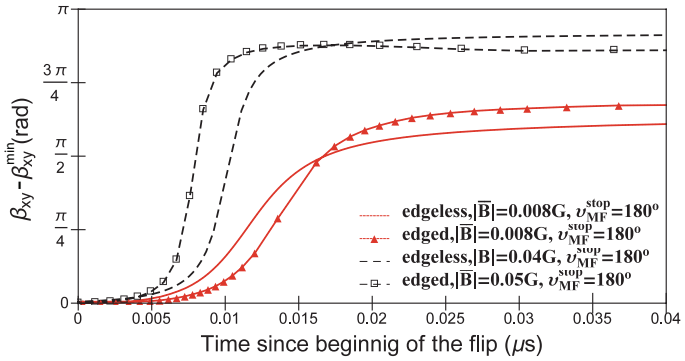

Fig. 11 Comparison of β_{xy} for simulations on edgeless vs edged discs (colour online). The discs have $R = 1.02\,\mu m$, $L = 0.0616\,\mu m$.

Though inclusion of the backflow effects in the simulation does not change the qualitative flipping behaviour, similar to edgeless discs, it changes the position of the disc before the beginning of the flip (Figure 9IVd and Figure 9Id). Figures 9II, III give more snapshots of the flip, where II has no backflow and III has backflow. From this figure it is easy to see that two discs start the flip at different positions, then during the flip one of them rotates clockwise and the other one - counter clockwise; then they finish at the same position (forced by magnetic field) but the disc that was also under action of backflow is a mirror image of the disc on Figure 9 (darker and lighter sides of the disc got switched). The quantitative analysis of rotational motion for both simulations, i.e. the time dependence of φ^{rot}, is similar to that shown in the inset of Figure 8: backflow leads to more rotation. The same dependence for other discs under action of various magnetic fields is demonstrated on Figure 10c.

These results show that the edged disc's flipping motion, position before and after the flip, and velocity of the flip can be controlled by only tuning the magnitude of magnetic field and its angular velocity. As for backflow effects, they are more important for edged discs than for edgeless discs. They change the disc's position before and after the flip, and the flipping motion itself by adding more rotation. Thus, for accurate predictions on the motion of the disc, backflow effects have to be taken into account for both edged and edgeless discs.

We also looked at how switching from an edgeless representation to the edged one changes the dynamics of the disc. In Figure 11 results for two discs are shown. Red dotted lines correspond to the discs of the same size ($R = 1.02\,\mu m$ and $L = 0.0616\,\mu m$) under the action of the same magnetic field ($0.008G$ that rotates $0.02^\circ/1\mu s$, i.e. 55.6Hz), but the one with filled triangles has a disc with additional particles on the cylindrical surface (edged representation, number of nodes in the object is 8534) compared to dotted line without any markers (edgeless disc consisting of 7250 nodes). As expected, the final position and the flip velocity has changed by shifting from the edgeless disc to the edged one, meaning that the anchoring on the edge of the disc affect the dynamics even for thin discs.

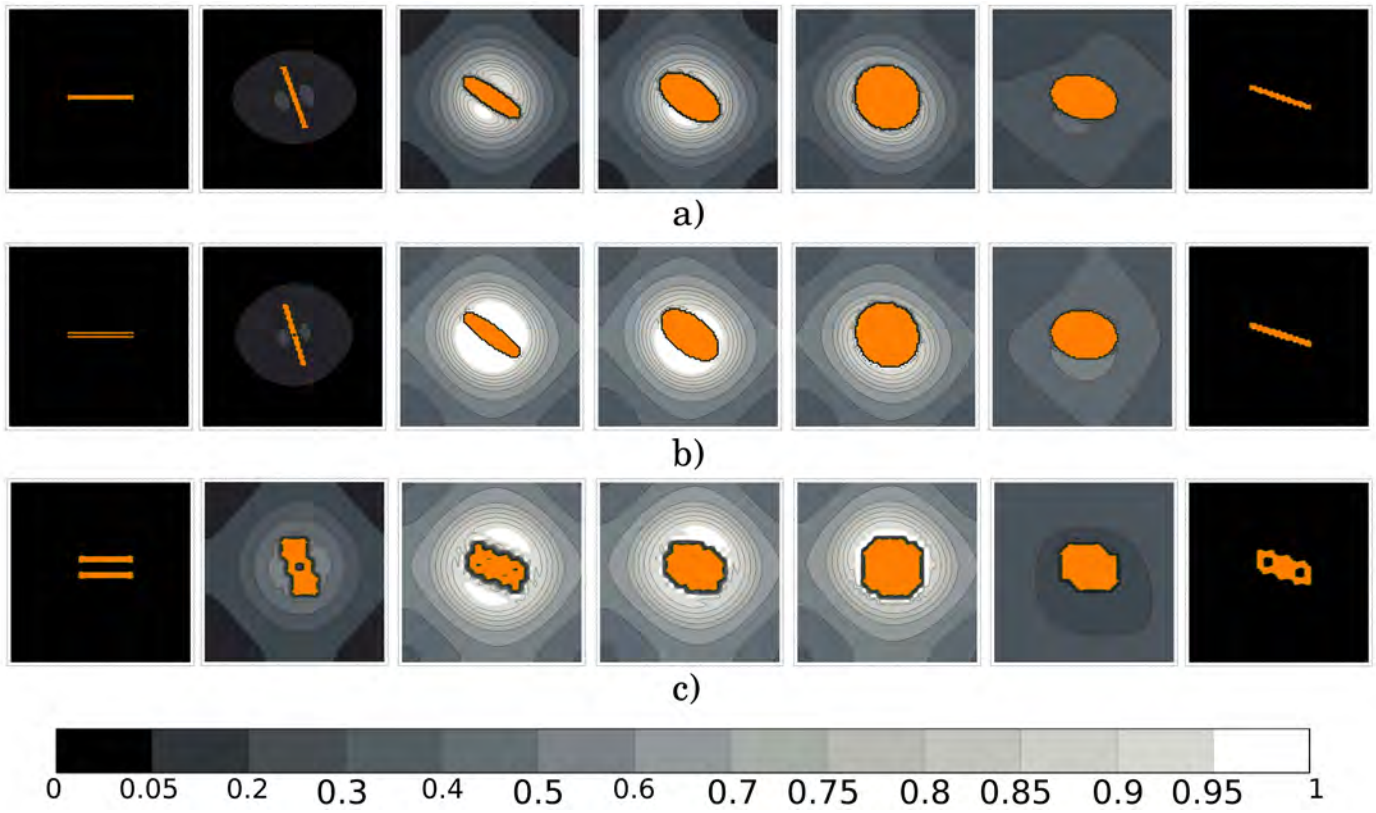

Fig. 12 Normalized intensity of light through the liquid crystal with the disc colloid in the middle (nodes of the disc are shown in orange) in crossed polarizers. On pictures (a) the results for an edged disc are presented ($R = 1.02\,\mu m$ and $L = 0.0616\,\mu m$ under action of magnetic field of magnitude $0.03G$ had a rotation frequency of 13.9Hz). Pictures in (b) correspond to an edgeless disc of the same size and same conditions. The set of pictures (c) corresponds to a simulation with an edgeless disc of $R = 0.3\,\mu m$ and $L = 0.15\,\mu m$ and magnetic field $0.03G$ with rotation frequency of 13.9Hz. Enlarged numbers on the gray scale are the values of plotted contours on both sets. Colour online.

3.3 Light transmission

To analyse the optical effects of the disc's flipping motion and to provide detailed interpretation of experimental results, the outgoing intensity of light through the liquid crystal sample with a disc in it was studied. Our approach, details of which can be found in Appendix B, has the advantage of choosing any view point (compared to experimental set-up) and provides the opportunity to study how the light transmission changes from plane to plane and is affected by distortion and defects. Simulations in this section do not include backflow effects.

Results of these calculations are presented in Figure 12. Black means that no light is getting through, while white corresponds to transmittivity close to 100%. The distortion changes the amount of light that goes through the area resulting in light grey areas. This results can be compared to experimental pictures produced by Rovner *et.al.*[38]. It can be seen that results of the simulations with edgeless discs presented on Figure 12b, c provide a picture similar to the experimental ones and give the details of the level of distortion in the area close to the disc surface. One notices the area corresponding to the value of normalized intensity $0.95 - 1$ that appears right after the flip starts. The disc performs the flipping motion inside this area, which firstly grows and then shrinks back to the surface of the disc during the flip and disappears when the flip is completed. However the pictures for the edged discs (Figure 12a) are different: the shell does not appear and the distortion stays closer to the surface of the particle. The defects on the edge of the disc "consume" part of the distortion and, thus, do not let it spread. Therefore, we can conclude, that the chemical treatment of the disc particle in the experiments of Rovner and co-workers[38] didn't set strong or medium-strong perpendicular surface anchoring on the edge of the disc but rather set it either weak or left unchanged. Also their "defect" is probably an effect of the director changing from in-plane to out-of-plane as seen in Figure 4I. This will look similar to a defect line under the microscope, as we see here.

3.4 Rapidly rotating magnetic field

All results discussed so far are for situations when the magnetic field was rotating fairly slowly. In this case both edged and edgeless discs rotate following the magnetic field and at an angle θ_{crit} flip around the axis perpendicular to the axis of rotation. However, different behaviour was observed for rapidly rotating magnetic fields for discs of both types of representation, edgeless and edged. Here "slowly" and "rapidly" angular velocities are relative and somewhat different for each disc depending on the type of representation, disc size and magnitude of magnetic field. At high rotational velocities when the angle of the disc's rotation θ become greater then $\pi/2$ and distortion around the disc grows, two

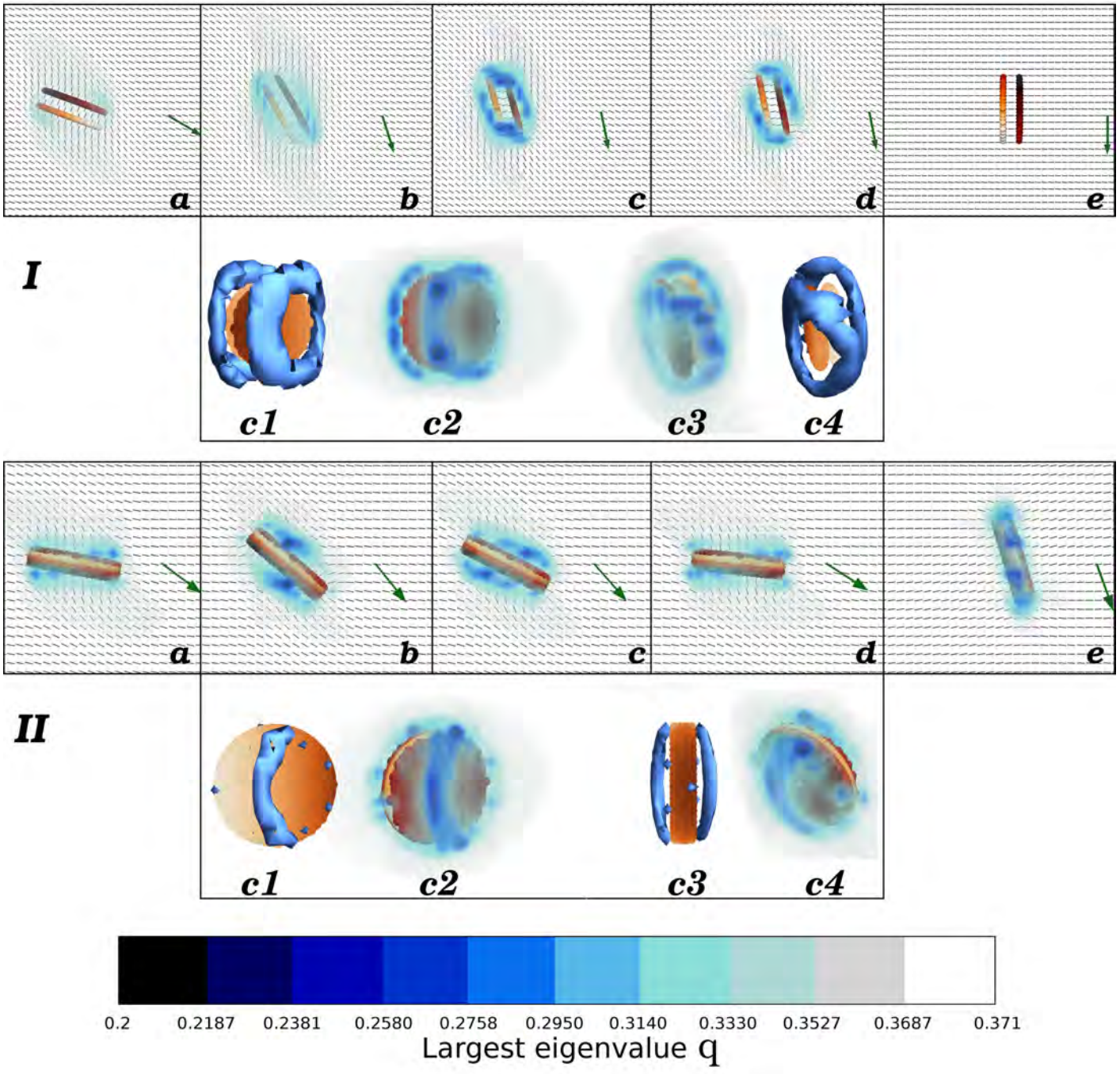

Fig. 13 Snapshots of the top view of the simulations of edgeless (a) and edged (b) discs under action of a rapidly rotating magnetic field. The disc is shown in dark-to-light orange colours (disc is represented by spheres located at the positions of the nodes; the spheres are made about 2 times larger than the real node size for better visibility), and a green arrow represents the direction of magnetic field. Level of distortion is represented as color density plot of the largest eigenvalue of tensor order parameter q. Here dark blue areas indicate the position of a disclination line defect (discontinuities in this line are a result of the graphic projection: the line is a physically continuous loop around the edge of the disc), light blue contour around the defects is a high level of distortion ("softening"), and grey cloud exhibits a light disturbance. Additional pictures c1-c2 on I and II corresponds to the side views of snapshots number Ic and IIc and include sharper contours to better illustrate the shape of the defect lines. See Supplemental Material for videos of the simulation.

symmetrical defects are formed on both sides of the disc (see Figure 13Ic and IIc). As can be seen from pictures Ic1-Ic2 and IIc1-IIc2 (the side views of the snapshots Ic and IIc), the defect for an edgeless disc is D-shaped, while the defect around the edged disc is C-shaped. The formation of the defects is probably due to the inability of the liquid crystal medium away from the edge to react rapidly to the changes in the orientation of the disc. After these defects are formed, they affect the liquid crystal director farther from the edge of the disc and reorient particles in that area leading to the disappearing of the S-shaped distortion (Figure 13Id and IIc) and relaxation of the distortion without flipping of the disc. After that, the disc aligns itself with the magnetic field (Figure 13Ie and IIe). Simulations from Figure 13 were performed with backflow, however this behaviour was tested in simulations without backflow effects and similar results were obtained.

4 Discussions

To conclude, in this paper we numerically study the behaviour of a disc-shape ferromagnetic colloidal particle in the nematic phase of a liquid crystal and demonstrate good agreement with experiments. In this work we demonstrate how to measure the capacitance of an immersed disc particle with knowledge of the values of elastic constants of the liquid crystal. Or, vice versa, one could define the elastic properties of the liquid crystal if the capacitance of the immersed disc colloid is known.

At small deviations from the initial configuration due to a slowly rotating magnetic fields the distortion of the director field can be predicted with help of equation (13). At large deviations it is hard to analytically predict the motion of the disc. In this work we have shown that the behaviour under this situation can be controlled by the angular speed of the magnetic field and its magnitude. During our investigation, we showed that (i) the critical flipping angle depends on the angular velocity of the magnetic field and its magnitude, (ii) for slowly rotating magnetic fields no defects are formed during the whole rotational and flipping motion (except for the areas at the edges of the disc due to the conflict in surface conditions),(iii) the distortion during the flip stays mainly inside a softening cloud, (iv) the size of the cloud strongly depends on the twist elastic constant of the liquid crystal and whether or not the anchoring is effective on the edge of the disc, (v) the light transmission is strongly affected by the director pointing out of plane during the flip and this can give the (false) impression of a disclination line where the director is perpendicular to the plane of observation, (vi) the flip may be avoided by increasing the rotational velocity of the magnetic field, (vii) backflow effects are vital for calculations, while net forces may be neglected as the centre-of-mass does not move appreciably. To sum up, this suggests a potential new approach for controlling colloidal interactions in liquid crystals and optical properties of colloidal discs sets. We also want to emphasise that our results suggest the edgeless disc representation better fits the experiments than the edged representation for chemical treatments similar to the one performed by Rovner *et.al.*[38]. After performing analysis of light transmission we can conclude that the line around the disc seen in the experiment that was interpreted as a defect is actually the edge of the area where the director is pointing out of plane.

Our code provides the opportunity to work with disc-shaped particles with different aspect ratio as well, making it possible to work with not only thin discs but also with rod-shaped particles, laths, etc. Also the code can be modified to be used for more complicated shapes such as torus, ring, hollow cylinder.

In future work we plan to look at the interaction between multiple disc-shaped particles immersed in liquid crystals under the action of magnetic fields and study their behaviour and motion.

5 Acknowledgements

We would like to thank the Natural Science and Engineering Research Council of Canada (NSERC) for financial support. This research has been enabled by the use of computing resources provided by Shared Hierarchical Academic Research Computing Network (SHARCNet) and Compute/Calcul Canada.

We also thank Robert Leheny for helpful discussions.

A Appendix: Lattice Boltzmann Algorithm

The Lattice Boltzmann algorithm treats a liquid as a set of distributions existing on mesh sites. At each site, scalar partial distribution functions $f_i = f_i(\mathbf{x}, t)$ are defined, giving the probability to find particles at site $\mathbf{x}$ at time t with velocity $\mathbf{e_i}$ — discrete velocity vectors defined by the velocity model chosen for the simulation, the D3Q15 model in our case. For liquid crystal hydrodynamics we also need another set of distribution functions — symmetric traceless tensors $\mathbf{G}_i$ with a similar meaning to f_i to evaluate the tensor order parameter $\mathbf{Q}$. From these distribution functions the density, momentum, and $\mathbf{Q}$ are defined as[52]:

$$\rho = \sum_i f_i,\ \rho u_\alpha = \sum_i f_i e_{i\alpha},\ \mathbf{Q} = \sum_i \mathbf{G}_i. \tag{16}$$

The partial distribution functions evolve according to a velocity discretized version of linearized Boltzmann equation with BGK collision operator,

$$(\partial_t + e_{i\alpha}\partial_\alpha) f_i = -\frac{1}{\tau_f}(f_i - f_i^{eq}) + p_i, \tag{17}$$

where p_i is an external forcing term controlling external force F_α, and τ_f is the relaxation parameter related to the fluid viscosity. To solve equation (17), algorithm suggested by Ollila et.al.[53] was used, which gives

$$\begin{aligned} f_i(\mathbf{x} + \mathbf{e_i}\triangle t, t + \triangle t) &= e^{-\Delta t/\tau_f} f_i(\mathbf{x}, t) + \Upsilon_f \tilde{f}_i^{eq}(\mathbf{x}, t) \\ &+ (\Delta t - \tau_f \Upsilon_f) D_i \tilde{f}_i^{eq}(\mathbf{x}, t) \\ &+ (\tau^2 \Upsilon_f - \Delta t \tau_f + \Delta t^2/2) D_i^2 \tilde{f}_i^{eq}(\mathbf{x}, t) + \mathcal{O}(\Delta t^4) \end{aligned} \tag{18}$$

with $\Upsilon_f = 1 - e^{-\Delta t/\tau_f}$ and

$$\begin{aligned}
&\tilde{f}_i^{eq} = f_i^{eq} + \tau_f p_i,\\
&D_i \tilde{f}_i^{eq}(\mathbf{x},t) = \frac{\tilde{f}_i^{eq}(\mathbf{x},t) - \tilde{f}_i^{eq}(\mathbf{x}-\mathbf{e}_i\Delta t, t-\Delta t)}{\Delta t},\\
&D_i^2 \tilde{f}_i^{eq}(\mathbf{x},t) = \frac{\tilde{f}_i^{eq}(\mathbf{x}+\mathbf{e}_i\Delta t, t) - \tilde{f}_i^{eq}(\mathbf{x},t)}{\Delta t^2}\\
&\quad - \frac{\tilde{f}_i^{eq}(\mathbf{x},t-\Delta t) + \tilde{f}_i^{eq}(\mathbf{x}-\mathbf{e}_i\Delta t, t-\Delta t)}{\Delta t^2}.
\end{aligned} \tag{19}$$

Equation (18) was obtained from a Taylor series expansion of $\tilde{f}_i^{eq}$ about $s = 0$ in the exact solution of equation (17) at $t + \Delta t$:

$$\begin{aligned}
f_i(\mathbf{x}+\mathbf{e}_i\Delta t, t+\Delta t) = e^{-\Delta t/\tau_f}\Big(f_i(\mathbf{x},t) +\\
\int_t^{t+\Delta t} \frac{1}{\tau_f} e^{(s-t)/\tau} \tilde{f}_i^{eq}(\mathbf{x}+\mathbf{e}_i\Delta s, t+s) ds\Big).
\end{aligned} \tag{20}$$

Similarly, the equation to evolve $\mathbf{Q}$ can be written

$$(\partial_t + e_i \cdot \nabla)\mathbf{G}_i = -\frac{1}{\tau_G}(\mathbf{G}_i - \mathbf{G}_i^{eq}) + \mathbf{M}_i, \tag{21}$$

together with the solution

$$\begin{aligned}
\mathbf{G}_i(\mathbf{x}+\mathbf{e_i}\triangle t, t+\triangle t) = e^{-\Delta t/\tau_G}\mathbf{G}_i(\mathbf{x},t) + \Upsilon_G \tilde{\mathbf{G}}_i^{eq}(\mathbf{x},t)\\
+ (\Delta t - \tau_G\Upsilon_G) D_i \tilde{\mathbf{G}}_i^{eq}(\mathbf{x},t)\\
+ (\tau_G^2\Upsilon_G - \Delta t\tau_G + \Delta t^2/2) D_i^2 \tilde{\mathbf{G}}_i^{eq}(\mathbf{x},t)\\
+ \mathcal{O}(\Delta t^4),
\end{aligned} \tag{22}$$

where $\Upsilon_G = 1 - e^{-\Delta t/\tau_G}$. Expressions for $\tilde{\mathbf{G}}_i^{eq}$, $D_i\tilde{\mathbf{G}}_i^{eq}$ and $D_i^2\tilde{\mathbf{G}}_i^{eq}$ are similar to (19). The form of the equations of motion and thermodynamic equilibrium follow from the restrictions on the moments of the distribution functions f_i^{eq} and $\mathbf{G}_i^{eq}$ and the driving terms $p_i(\mathbf{x},t,\{f_i\})$ and $\mathbf{M}_i(\mathbf{x},t,\{\mathbf{G_i}\})$. Full details on the algorithm can be found in Ref.[54].

B Appendix: Light Transmission

To study light transmission, each simulation layer of the liquid crystal along the z direction was considered to be a polariser with the input amplitude of light $\bar{A}_{in}^s = \bar{i}_{||}A_{in}^s + \bar{j}_{\perp}A_{in}^s$ defined at each point (i,j) of the site mesh on the layer s consisted of a component $_{||}A^s$ in the x direction and $_{\perp}A^s$ in the y direction and output amplitude $\bar{A}_{out}^s = \bar{i}_{||}A_{out}^s + \bar{j}_{\perp}A_{out}^s$ calculated via

$$\begin{aligned}
\bar{A}_{out}^s = (\bar{A}_{in}^{s-1}\cdot\hat{b}^{s-1})\hat{b}^{s-1} +\\
(\bar{A}_{in}^{s-1}\cdot(J\hat{b}^{s-1}))(J\hat{b}^{s-1})(1-q)cos^2\theta.
\end{aligned} \tag{23}$$

$\bar{A}_{out}^s$ is at the same time the input amplitude for the next layer (see Figure 14). Here $\hat{b}$ is a projection of the director $\hat{n}^s$ at the site mesh (i,j) on the xy-plane, θ is the angle between the z-axis and director, q is the corresponding eigenvalue of the tensor order parameter $\mathbf{Q}$, J is orthogonal matrix. On the 0^{th} layer $\bar{A}_{out}^0 = \bar{i}_{||}A_{out}^0$ due to the presence of the light polariser (or $\bar{A}_{out}^0 = \bar{i}_{\perp}A_{out}^0$ depending on the type of polariser). And, similarly, on the last $N+1$ layer where another polariser is located, depending on if it is crossed with the first one or not, the output amplitude is $\bar{A}_{out}^{N+1} = \bar{i}_{||}A_{out}^N$ or $\bar{A}_{out}^{N+1} = \bar{i}_{\perp}A_{out}^N$. If the disc is found to be on the way of the light beam, the tranmitted light is extinguished and $\bar{A}_{out} \equiv 0$ at this (i,j). Finally, the intensity of the light that got through the liquid crystal sample is calculated as square of the amplitude from the last layer.

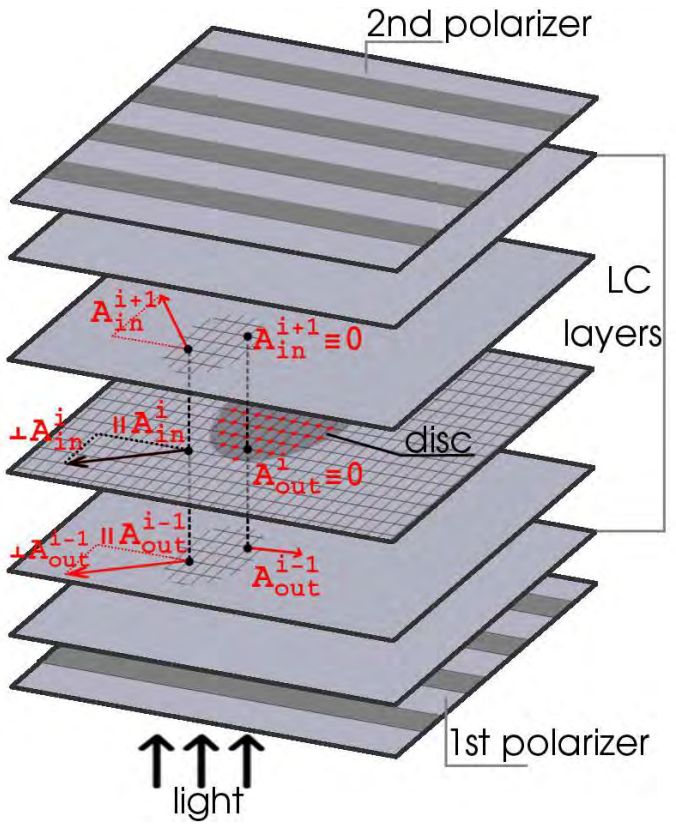

Fig. 14 The calculation scheme of the intensity of light, going through the liquid crystal with disc represented by the red dots immersed in it (colour online).

References

1 S. V. Burylov and Y. L. Raikher, *Phys. Rev. E*, 1994, **50**, 358–367.
2 E. M. Terentjev, *Phys. Rev. E*, 1995, **51**, 1330–1337.
3 R. W. Ruhwandl and E. M. Terentjev, *Phys. Rev. E*, 1997, **56**, 5561–5565.
4 P. Poulin, H. Stark, T. C. Lubensky and D. A. Weitz, *Science*, 1997, **275**, 1770–1773.
5 P. Poulin and D. A. Weitz, *Phys. Rev. E*, 1998, **57**, 626–637.
6 T. C. Lubensky, D. Pettey, N. Currier and H. Stark, *Physical Review E*, 1998, **57**, 610–625.
7 O. Mondain-Monval, J. Dedieu, T. Gulik-Krzywicki and P. Poulin, *The European Physical Journal B - Condensed Matter and Complex Systems*, 1999, **12**, 167–170.
8 H. Stark, *The European Physical Journal B - Condensed Matter and Complex Systems*, 1999, **10**, 311–321.

9 H. Stark, *Physics Reports*, 2001, **351**, 387 – 474.

10 F. E. Mackay and C. Denniston, *Soft Matter*, 2013, **9**, 5285–5292.

11 F. E. Mackay and C. Denniston, *EPL*, 2011, **94**, 66003.

12 I. Musevic and M. Škarabot, *Soft Matter*, 2008, **4**, 195–199.

13 Q. Liu, B. Senyuk, M. Tasinkevych and I. I. Smalyukh, *Proceedings of the National Academy of Sciences*, 2013, **110**, 9231–9236.

14 J.-C. Loudet, P. Barois and P. Poulin, *Nature*, 2000, 611–613.

15 M. Yada, J. Yamamoto and H. Yokoyama, *Physical review letters*, 2004, **92**, 185501.

16 I. Muševič, M. Škarabot, U. Tkalec, M. Ravnik and S. Žumer, *Science*, 2006, **313**, 954–958.

17 F. E. Mackay and C. Denniston, *Soft Matter*, 2014, **10**, 4430–4435.

18 C. M. Lieber, *MRS Bulletin*, 2003, **28**, 486–491.

19 Y. Li, F. Qian, J. Xiang and C. M. Lieber, *Materials Today*, 2006, **9**, 18 – 27.

20 L. A. Bauer, N. S. Birenbaum and G. J. Meyer, *J. Mater. Chem.*, 2004, **14**, 517–526.

21 A. Kolmakov and M. Moskovits, *Annual Review of Materials Research*, 2004, **34**, 151–180.

22 P. J. Pauzauskie and P. Yang, *Materials Today*, 2006, **9**, 36 – 45.

23 M. Škarabot, M. Ravnik, S. Žumer, U. Tkalec, I. Poberaj, D. Babič, N. Osterman and I. Muševič, *Phys. Rev. E*, 2008, **77**, 031705.

24 C. J. Smith and C. Denniston, *Journal of Applied Physics*, 2007, **125**, 014305.

25 C. P. Lapointe, D. H. Reich and R. L. Leheny, *Langmuir*, 2008, **24**, 11175–11181.

26 A. Anguelouch, R. L. Leheny and D. Reich, *Applied Physics Letters*, 2006, **89**, 111914–111914–3.

27 C. Lapointe, A. Hultgren, D. M. Silevitch, E. J. Felton, D. H. Reich and R. L. Leheny, *Science*, 2004, **303**, 652–655.

28 N. Cappallo, C. Lapointe, D. H. Reich and R. L. Lapointe, *Phys. Rev. E*, 2007, **76**, 031505.

29 P. van der Schoot, V. Popa-Nita and S. Kralj, *The Journal of Physical Chemistry B*, 2008, **112**, 4512–4518.

30 C. Lapointe, N. Cappallo, D. H. Reich and R. L. Leheny, *Journal of Applied Physics*, 2005, **97**, 10Q304.

31 M. Tasinkevych, F. Mondiot, O. Mondain-Monval and J.-C. Loudet, *Soft Matter*, 2014, **10**, 2047–2058.

32 F. Mondiot, S. P. Chandran, O. Mondain-Monval and J.-C. Loudet, *Phys. Rev. Lett.*, 2009, **103**, 238303.

33 M. D. Lynch and D. L. Patrick, *Nano Letters*, 2002, **2**, 1197–1201.

34 C. P. Lapointe, S. Hopkins, T. G. Mason and I. I. Smalyukh, *Physical review letters*, 2010, **105**, 178301.

35 C. P. Lapointe, T. G. Mason and I. I. Smalyukh, *Science*, 2009, **326**, 1083–1086.

36 P. G. de Gennes and J. Prost, *The Physics of Liquid Crystals*, Oxford University Press, Oxford, 2nd edn, 1993.

37 F. Brochard and P. de Gennes, *J. Phys. France*, 1970, **31**, 691–708.

38 J. B. Rovner, D. S. Borgnia, D. H. Reich and R. L. Leheny, *Phys. Rev. E*, 2012, **86**, 041702.

39 M. Doi and S. F. Edwards, *The Theory of Polymer Dynamics*, Clarendon Press, Oxford, 1989.

40 A. Beris and B. Edwards, *Thermodynamics of Flowing Systems*, Oxford University Press, 1994.

41 M. Yakutovich, C. Care, C. Newton and D. Cleaver, *Phys Rev E Stat Nonlin Soft Matter Phys*, 2010, **94**, 041703.

42 C. Denniston, E. Orlandini and J. M. Yeomans, *Phys. Rev. E*, 2001, **63**, 056702.

43 F. Mackay and C. Denniston, *Journal of Computational Physics*, 2013, **237**, 289 – 298.

44 F. Mackay, S. Ollila and C. Denniston, *Computer Physics Communications*, 2013, **184**, 2021 – 2031.

45 S. Plimpton, *Journal of Computational Physics*, 1995, **117**, 1–19.

46 S. Chandrasekhar, *Liquid Crystals*, Oxford University Press, Cambridge, 2nd edn, 1992.

47 P. M. Morse and H. Feshbach, *Methods of theoretical physics*, McGraw-Hill Science/Engineering/Math, 1953.

48 S. Ollila, C. Smith, T. Ala-Nissila and C. Denniston, *Multiscale Model. Simul.*, 2013, **11**, 213–243.

49 G. Tóth, C. Denniston and J. M. Yeomans, *Phys. Rev. Lett.*, 2002, **88**, 105504.

50 C. Denniston, G. Tóth and J. Yeomans, *Journal of Statistical Physics*, 2002, **107**, 187–202.

51 G. Tóth, C. Denniston and J. M. Yeomans, *Computer Physics Communications*, 2002, **147**, 7–12.

52 S. Chen and G. D. Doolen, *Annual Review of Fluid Mechanics*, 1998, **30**, 329–364.

53 S. T. T. Ollila, C. Denniston, M. Karttunen and T. Ala-Nissila, *J. Chem. Phys.*, 2011, **134**, 064902.

54 C. Denniston, E. Orlandini, J. M. Yeomans and D. Marenduzzo, *Philosophical Transactions of the Royal Society of London. Series A:Mathematical, Physical and Engineering Sciences*, 2004, **362**, 1745–1754.